In-cell Detection of Conformational Sub-states of a GPCR Quaternary Structure: Modulation of Sub-state Probability by Cognate Ligand Binding

Joel Paprocki[1], Gabriel Biener[1], Michael Stoneman[1], Valerica Raicu[1,2,*]

[1]Department of Physics, [2]Department of Biological Sciences, University of Wisconsin-Milwaukee, Wisconsin, USA

ABSTRACT

While the notion that G protein-coupled receptors (GPCRs) associate into homo- and hetero-oligomers has gained more recognition in recent years, a lack of consensus remains among researchers regarding the functional relevance of GPCR oligomerization. A technique, Förster resonance energy transfer (FRET) spectrometry, allows for the determination of the oligomeric (or quaternary) structure of proteins in living cells via analysis of efficiency distributions of energy transferred from optically excited fluorescent tags acting as donors of energy to fluorescent tags acting as acceptors of energy and residing within the same oligomer. In this study, we significantly improved the resolution of FRET-spectrometry to detect subtle differences in quaternary structures of GPCR oligomers within living cells. We then used this approach to study the conformational substates of oligomers of sterile 2 α-factor receptor (Ste2), a class D GPCR found in the yeast *Saccharomyces cerevisiae* of mating type **a**. Ste2 has previously been shown to form tetramers at relatively low expression levels (11 to 140 molecules/μm^2) in the absence of its cognate ligand, the α-factor pheromone. The significantly improved FRET spectrometry technique allowed us to detect multiple distinct quaternary conformational substates of Ste2 oligomers, and to assess how the α-factor ligand altered the proportion of such substates. The ability to determine quaternary structure substates of GPCRs provides exquisite means to elucidate functional relevance of GPCR oligomerization.

*Corresponding author's email address: vraicu@uwm.edu

1. INTRODUCTION

G protein-coupled receptors (GPCRs) are a family of membrane-bound proteins which recognize and respond to a gamut of extracellular stimuli, thereby modulating the dissociation of the trimeric G protein from the cytoplasmic side of the receptor and inducing down-stream signaling events[1,2]. GPCRs have traditionally been divided into six different classes according to their amino acid sequence and functional similarity: Class A-rhodopsin-like receptors, Class B-secretin family, Class C-metabotropic glutamate receptors, Class D-fungal mating pheromone receptors, Class E-cAMP receptors, and Class F-frizzled (FZD) and smoothened (SMO) receptors[3].

Mounting evidence from a plethora of experiments, both in vitro and in living cells, indicates that GPCRs may form homo- or hetero-oligomeric complexes[4-11]. However, the prevalence and functional significance of such oligomeric complexes remains a largely open question. For some GPCRs, such as those belonging to the Class C-metabotropic glutamate subfamily, homo or hetero-oligomerization is absolutely essential for activation of the receptor[12]. By contrast, a number of other GPCRs, e.g., the β_2-adrenoceptor, have been shown to retain functionality in monomeric form[13-15], although they are also capable of forming dimers and/or higher order oligomers[16]. It would appear from these varied results that the degree of oligomerization, as it relates to function, may be class-specific, if not receptor-specific, although this remains quite unclear. In this regard, reliable methods that can report on the quaternary organization (i.e., oligomer geometry and interprotomeric distances) of GPCRs and specify how these structures are altered in response to activation by ligand binding are needed for a better understanding of the physiological relevance of GPCR oligomerization.

Fluorescence-based methods, particularly those which rely on Förster Resonance Energy Transfer (FRET), have been very effective in quantifying the interactions of membrane receptors within living cells. In FRET studies, the membrane proteins of interest are tagged with two fluorescent labels: a “donor” (D) and an “acceptor” (A). If the two fluorescent molecules reside within 10 nm of one another, a radiationless transfer of energy can occur from an optically excited D molecule to an unexcited A molecule[17]. The efficiency of the radiationless energy transfer is strongly dependent on the distance between the fluorophores, and therefore quantification of the FRET efficiency occurring between membrane protein labels reveals information about the relative proximity, and thereby interactions, of the receptors themselves[5,18-22]. If prior knowledge exists regarding the oligomeric size (i.e., number of protomers) and geometry (i.e., relative

distances between protomers), then ensemble-average-based FRET approaches allow one to determine relative proportions of monomers and different sized oligomers[23-26].

A more recent addition to the family of FRET methods, FRET spectrometry[27,28], can provide the size and geometrical parameters of the underlying quaternary structure of the receptor of interest. In FRET spectrometry, pixel-level values of FRET efficiency are assembled into distributions, or FRET spectrograms, from which the most frequently occurring FRET efficiency values (i.e., peaks) are extracted. A collection of the dominant histogram peaks is then assembled into another histogram, termed a *meta-histogram*, to further separate the information originating from mixtures of oligomers with different sizes and geometries. To determine the size and shape of oligomers from meta-histograms, an data fitting process is performed which requires rigorous tests of how well various oligomer models simulate the measured meta-histogram[27,29].

A number of methods, both experimental (e.g., fluorescence spectroscopy and crystallography) and computer-based (i.e., molecular dynamics simulations), which are well suited to study the tertiary structure of membrane receptors have shown that individual GPCRs are not rigid structures, but dynamic in nature, switching between multiple conformational substates[30-33]. It is therefore reasonable to expect that these fluctuations in the tertiary structure would lead to various quaternary structure substates as well. However, previous FRET spectrometry studies have been limited to determining only an average or most probable quaternary structure[27,29].

In the work described herein, we have significantly improved the resolution of FRET spectrometry so that it can resolve even slight alterations in the distance between protomers within the quaternary structure (i.e., less than 1 Å). The necessary improvement in resolution and sensitivity was accomplished, firstly, by isolating membrane-only regions of interest in the acquired images, and further dividing these regions into smaller segments. In this way, we capture fluctuations in quaternary structure between regions of the membrane which were previously smoothed out in the process of data analysis. Secondly, we refined our previous method of estimating the receptor concentrations (using two different excitation wavelengths)[27,34] which allowed us to select subsets of the FRET spectrograms from cells expressing receptors in a narrow concentration range, to further sample the fluctuations of the receptor quaternary structure. This data acquisition strategy, combined with other methodological improvements and implementation of a noise-filtering algorithm, enabled a new picture to emerge of the quaternary structure versatility, which has never been observed in living cells. Specifically, we detected the presence

of several quaternary structure conformations (or substates) in a typical class D GPCR, the sterile 2 α-factor pheromone receptor (Ste2), in the presence and absence of its cognate ligand[27,35-40].

Ste2 is found in the yeast *Saccharomyces cerevisiae*[41-44] of the mating type **a**. The receptor binds the α-factor pheromone, which is secreted from cells of mating type **α**, and subsequently initiates the signaling response, leading to the mating of haploid **a** and **α** cells[45-47]. Previous publications revealed that the Ste2 receptor forms complexes as large as tetramers at relatively low concentrations[6,48,49]. In our most recent study of Ste2 oligomerization[27], we found that it forms tetramers at concentrations as low as 11 receptors/μm^2, with some octamers starting to form at higher concentrations of at least 140 receptors/μm^2. In studies of other GPCRs, sizeable fractions of dimers have been detected even at concentrations 100 times lower than those available in the present investigation[50,51], while addition of ligand has been shown to markedly increase the fraction of dimers or higher order oligomers[50,52,53]. While Ste2 is well characterized as a prototypical model for extracellular sensing, previous studies mainly focused on determination of the quaternary structure of Ste2 in the absence of ligand and also lacked the necessary resolution to detect changes in the oligomer conformation[27].

In this study, we were able to resolve, for the first time in living cells, four different quaternary structure conformations (or substates) of Ste2, which were characterized by different distances between the protomers within the oligomer. We attribute this finding to the fact that the individual protomers comprising the oligomer can exist in multiple semi-stable, low-energy-state conformations, as is known from studies focusing on tertiary structures of other GPCRs[2,54-58]. Furthermore, upon addition of ligand, the relative abundance of the quaternary conformations was shifted from the Ste2 structure primarily being characterized by the smallest interprotomeric distances to substates with larger distances, suggesting that quaternary structure sub-states might be related to biological function. These studies may be expanded to include other GPCRs (or any other membrane receptor) which may be exposed to different natural and artificial ligands, and thus significantly aiding in the search for the physiological relevance of GPCR oligomerization.

2. MATERIALS AND METHODS

2.1 Sample Preparation

Baker's yeast cells (*Saccharomyces cerevisiae*) were engineered to express the sterile 2 α-factor pheromone receptor (Ste2) fused to one of two different fluorescent tags, i.e. GFP_2[59] or YFP[60,61] at

position 304 in the Ste2 amino acid sequence as previously described[27]. Yeast cells transformed with one or both of the plasmids were grown at 30 ºC on an agar-based plasmid selective synthetic complete medium lacking uracil and/or tryptophan.

Cell imaging was performed using 35-mm glass-bottom dishes (P35G-0.170-14-C, MATTEK Corporation, Ashland, MA). Prior to cell addition, the dishes were coated with concanavalin A (Sigma Aldrich, St. Louis, MO) to immobilize cells on the glass. To coat the dishes, 100 µL of a 0.5 mg/mL solution of concanavalin A (in deionized water) was placed on the coverslip of each dish. The dishes were then covered and incubated for 30 min at room temperature to allow deposition of the concanavalin A to occur. After 30 min, any remaining solution was removed, and the dishes were allowed to dry for a 24 h period prior to addition of cells.

Cells were scraped from the agar-based selective medium and suspended in 1 mL of 100 mM KCL buffer (pH 7.0). 200 µL of cell suspension was then pipetted onto the coverslip region of a concanavalin A coated glass-bottom dish and allowed to incubate for a period of 10 min. After the 10 minute incubation period, the dish was washed three times with 100 mM KCl buffer in order to remove any unbound cells, leaving a single layer of adherent cells for imaging[62]. For experiments where ligand effects were probed, an additional cell preparation step was introduced, as follows: A purified α-factor pheromone suspension (Y1001, Zymo Research, Irvine, CA) was diluted to a working concentration of 10 µM in 100 mM KCl to achieve and maintain saturation binding of ligand to receptors present within sample cell membranes[63,64]. Cells were suspended in 200 µL of the α-factor solution and allowed to incubate at room temperature for 5 min prior to plating. The incubated cell suspension was then added to a coated dish and incubated for another10 minutes to allow for the cells to adhere. After the incubation period, the dishes with adhered cells which had been exposed to ligand prior to plating were washed 3 times with the 10 µM ligand/buffer solution. After washing, the cell coated dishes were taken for imaging on a two-photon optical micro-spectroscope developed as described in the following section.

2.2 Two-photon fluorescence micro-spectroscopy

Fluorescence images were acquired using a spectrally resolved two-photon optical micro-spectroscope consisting of a tunable femtosecond laser (MaiTai^{TM}, Spectra Physics, Santa Clara, CA), an inverted microscope (Nikon Eclipse Ti^{TM}, Nikon Instruments Inc., Melville, NY) equipped with an infinity-corrected, plan apochromat, oil immersion objective (100×, NA=1.45; Nikon Instruments Inc.), and an OptiMiS scanning/detection head (Aurora Spectral Technologies,

Grafton, WI), as described previously[27,65]. The samples were scanned using a line-shaped excitation beam with a power of 0.2 mW/voxel and an integration time of 35 ms per pixel. Each field of view was scanned at two different excitation wavelengths, first at 930 nm and then 800 nm, for the purpose of obtaining the concentration of both acceptors and donors (see Section 2.4 below**)**. The total time needed to complete both excitation scans, including laser wavelength tuning time between scans, was ~60 s. The output of each excitation scan resulted in a set of micro-spectroscopic images which typically contained 200 different wavelength channels of ~1 nm bandwidth; the size of the image for each emission wavelength channel was 440 × 300 pixels[27]. (For one set of experiments which focused on samples with particularly low receptor concentrations, the wavelength channel width was increased to ~5 nm in order to increase the level of fluorescence signal relative to the readout noise of the detector.) Since molecular diffusion could potentially change the distribution of receptors and their oligomeric sizes for a given pixel during the relatively long time elapsed between each scan, both the donor and acceptor concentrations were computed as an average over a given region of interest rather than at pixel level.

2.3 Calculation of apparent FRET efficiency and assembly of meta-histograms

The composite emission spectrum from each pixel in the micro-spectroscopic images of cells co-expressing Ste2-GFP_2 and Ste2-YFP was deconvoluted into donor and acceptor components using a least-squares fitting algorithm along with separately determined elementary donor and acceptor emission spectra, as described elsewhere[66]. The elementary fluorescence spectrum of the donor (green fluorescent protein, GFP_2)[59] and the acceptor (yellow fluorescent protein, YFP)[60,61] were determined by acquiring micro-spectroscopic images of cells expressing either Ste2-GFP_2 or Ste2-YFP. Applying the unmixing procedure to each image pixel resulted in 2D maps of donor intensity in the presence of the acceptor, k^{DA}, and acceptor intensity in the presence of the donor, k^{AD}[66]. The k^{DA} and k^{AD} values are the coefficients multiplying each respective elementary spectrum composing the theoretical function used to fit the measured spectrum. The k^{DA} and k^{AD} values were multiplied with the area underneath their respective elementary spectrum (i.e., their spectral integrals) to obtain the total donor fluorescence emission in the presence of the acceptor, F^{DA}, and total acceptor emission in the presence of the donor, F^{AD} at each pixel within an image[6]. Spectral integrals for the donor ($w^D = 43.59$) and acceptor ($w^A = 42.92$) were found from averages of typical elementary spectra obtained over multiple experimental days. A single spectral integral was

used across multiple experiments in order to be able to compare receptor concentrations across multiple experimental days.

In the absence of acceptor direct excitation by laser light, the apparent FRET efficiency (E_{app}) may be determined from experiments using the following relationship[6,67]:

$$E_{app} = \frac{F^{AD}(\lambda_{ex2})}{\frac{Q^A}{Q^D}F^{DA}(\lambda_{ex2}) + F^{AD}(\lambda_{ex2})} \quad (1)$$

where $F^{AD}(\lambda_{ex2})$ is the fluorescence emission of the acceptors in the presence of donors upon excitation at a wavelength (λ_{ex2}) at which acceptors are not excited significantly (e.g., 800 nm), $F^{DA}(\lambda_{ex2})$ is the donor emission in the presence of acceptors excited at the same wavelength, $Q^D = 0.55$ is the quantum yield of the donor[59], and $Q^A = 0.61$ is the quantum yield of the acceptor[68]. As we shall explain in the next sub-section, while the donor concentration may be determined from the donor fluorescence (corrected for FRET) at the same wavelength ($\lambda_{ex2} = 800$ nm), the acceptor concentration determination requires an excitation scan at a different wavelength ($\lambda_{ex1} = 930$ nm).

A value of E_{app} was calculated for each pixel in a micro-spectroscopic image according to Eq. (1), for which a threshold criterion based on the calculated signal-to-noise ratio for both the donor and acceptor intensities in a given pixel (see Supplementary Methods section SM1) was then applied to the pixel-level maps of E_{app}. This means that the background-subtracted intensity of both the donor and acceptor signal had to be greater than or equal to the desired threshold value, *TH*, times the standard deviation of the noise in a given pixel, or the corresponding E_{app} value calculated for said pixel was rejected from further analysis. The *TH* was typically set to 1 for all experiments, except for a single experiment in which the wavelength channel width was set to 5 nm (see Section 2.2).

For certain pixels, the spectral unmixing resulted in an inadequate fit to the measured emission spectrum. In order to exclude these pixels from further analysis, we have introduced a second step of filtering, as follows. For every pixel within a micro-spectroscopic scan, the fit of the theoretical spectrum to the experimental one was quantified with the value $C(x, y)$, which was computed according to Eq. (S2). For each segmented polygon (see section 3.1 and Supplementary Methods section SM2), an average "goodness-of-fit" value was calculated by averaging the $C(x, y)$ values found for each pixel within the segment. Individual segments with an average goodness-of-fit value which was greater than a fixed goodness-of-fit criterion were not considered for further analysis, as described in Supplementary Methods section SM3. If a segment did pass

the goodness-of-fit criterion, the E_{app} values from each of the pixels falling within the segment were then organized into a histogram plot, or a FRET spectrogram[28,69], of bin width equal to 0.005. A FRET spectrogram was generated for each membrane segment in the set of images.

We further distilled the information contained within individual FRET spectrograms by extracting the positions of only the most prominent peaks within each spectrogram and generating a histogram of peak positions, i.e., a meta-histogram from the dominant peaks of multiple image segments[7,27,29]; the positions of the most prominent peaks were selected based on a routine described in detail in Supplementary Methods section SM4 and illustrated in Fig. S2. The total number of spectrograms used to generate each meta-histogram ranged from 100 to 300. The peak positions selected from individual FRET spectrograms were sorted based on the average receptor concentration (see section 2.4) of the corresponding segment such that meta-histograms were generated from peak values which originated from segments with the lowest overall concentration values.

As stated in the introduction, the meta-histogram is a collection of the E_{app} values from the most probable FRET-productive oligomeric complexes and is the basis for determining the quaternary structure in FRET spectrometry. Each meta-histogram was modeled using an oligomeric structure with a particular size and shape[70], as described in Supplementary Methods section SM5, in order to extract detailed information about the underlying receptor quaternary structure.

2.4 Estimation of receptor concentration for membrane cross-sections

The concentrations of donors and acceptors (in the presence of each other) within each membrane segment are proportional to the ratio of the would be fluorescence emission of the given fluorophore species *X* (i.e., *X* = D or A) in the absence of FRET and the fluorophore monomeric molecular brightness, $\varepsilon_{mon}^{X}(\lambda_{ex})$. The total fluorescence of each fluorophore species in the absence of FRET was determined from their measured fluorescence intensities obtained upon excitation at two different wavelengths, using the following relations[27,34,67]:

$$F^{A}(\lambda_{ex1}) = \left(F^{AD}(\lambda_{ex1}) - \frac{F^{AD}(\lambda_{ex2})}{\rho^{ex,D}}\right)\left(1 - \frac{\rho^{ex,A}}{\rho^{ex,D}}\right)^{-1} \quad (2)$$

$$F^{D}(\lambda_{ex2}) = F^{DA}(\lambda_{ex2}) + \frac{Q^{D}}{Q^{A}}F^{AD}(\lambda_{ex2}) - \frac{Q^{D}}{Q^{A}}\rho^{ex,A}F^{A}(\lambda_{ex1}) \quad (3)$$

where $F^D(\lambda_{ex2})$ is the fluorescence emission of the donor molecules corrected for the loss of emission due to FRET[6,70]. Similarly, $F^A(\lambda_{ex1})$ is the total emission of the acceptor molecules corrected for the gain in emission due FRET. The quantities $\rho^{ex,D}$ and $\rho^{ex,A}$ are the emission intensities upon excitation at λ_{ex2} relative to that at λ_{ex1} for a cell sample expressing donors and acceptors, respectively.

The method for determining the molecular brightness values for donors and acceptors is briefly presented below; for a more detailed description, see Supplementary Methods section SM7. Micro-spectroscopic measurements were performed on solutions of purified GFP_2 and YFP fluorescent proteins at a number of concentrations, a process which has been previously described[27]. The same excitation wavelengths, power, and exposure times used to measure the yeast cells were applied to the fluorescent protein solution measurements. Calibration curves were generated for both the GFP_2 and YFP solutions by plotting the average fluorescence intensity of the various solutions vs. the corresponding concentration. The slope, $p_{sol}^X(\lambda_{ex})$, of the calibration plot represents the amount of fluorescence signal detected per molar concentration of fluorescent protein, and is proportional to the molecular brightness, $\varepsilon_{mon}^X(\lambda_{ex})$, of a monomeric form of the respective fluorophore (see Eq. S11). The superscript *X* in the slope and molecular brightness symbols denotes either donor, *D*, or acceptor, *A*. The molecular brightness of the donors was found using an excitation wavelength of $\lambda_{ex2} = 800$ nm, and for the acceptors at $\lambda_{ex1} = 930$ nm.

The concentrations of the *D* or *A* fluorophores in the plasma membrane, C_{mem}^X, and the average measured fluorescence, obtained by averaging the pixel level values of $F^A(\lambda_{ex1})$ or $F^D(\lambda_{ex2})$, calculated in Eq. (2) and (3) respectively, within a single polygon segment was calculated as follows:

$$C_{mem}^D = \frac{\langle F^D(\lambda_{ex2})\rangle \cdot FWHM \cdot l}{p_{sol}^D(\lambda_{ex2})} \tag{4}$$

$$C_{mem}^A = \frac{\langle F^A(\lambda_{ex1})\rangle \cdot FWHM \cdot l}{p_{sol}^A(\lambda_{ex1})} \tag{5}$$

where $l = 0.16\ \mu m$ represents the length of a single camera pixel when projected onto the sample plane. Because fluorescence emission from the membrane region is spread over multiple pixels of the detector, $\langle F^X(\lambda_{ex})\rangle$ must be multiplied by $FWHM$, which represents the width in pixels of the emission PSF along the direction in which the signal is spread. According to Eq. (4) and (5), the average concentration (in molecules/μm^2) of receptors tagged with a particular fluorophore (i.e.,

either *D* or *A*) within a given segment can be found by averaging the fluorescence intensity values of the corresponding fluorophore over all the pixels in the segment. Therefore, to find the total receptor concentration in a given segment, we must add the average concentrations of receptors tagged with both donor and acceptor:

$$C_{mem}^{Total} = C_{mem}^{D} + C_{mem}^{A} \quad (6)$$

The values of C_{mem}^{Total} found for the segments used to compile the meta-histograms used in this study ranged from 11 to 211 receptors/μm^2.

Using a simple relation between the measured fluorescence intensities and molecular brightness[71], $\langle F^X(\lambda_{ex})\rangle = \frac{\varepsilon_{mon}^X(\lambda_{ex})\cdot N_X}{FWHM}$, as well as the relation between molecular brightness and $p_{sol}^X(\lambda_{ex})$, given in Eq. (S11), we can calculate the average number of donors or acceptors per pixel:

$$N_X = \frac{\langle F^X(\lambda_{ex})\rangle \cdot FWHM \cdot\cdot l \cdot \iint_{-\infty}^{\infty} PSF_{line}^2(y,z)\,dy\,dz}{p_{sol}^X} \quad (7)$$

where $PSF_{line}(y,z)$ represents the spatial profile of the line shaped excitation beam, which is uniform along a single dimension (which we have denoted as the *x*-dimension in the theoretical formulation given in Supplementary section SM7).

In Eq. (7), we estimate the number of receptors tagged with a particular fluorophore contained within a volume corresponding to a single image pixel. The total number of receptors, N_{Total}, in a single pixel is then found by adding the number of donor-tagged and acceptor-tagged receptors found for said pixel, i.e., $N_{Total} = N_D + N_A$. For the concentration range used to assemble the meta-histograms in this study (9 to 203 receptors/μm^2) the corresponding range of N_{Total} values was 8-183 receptors/pixel.

3. RESULTS

3.1. Preliminary assessment of FRET efficiency meta-histograms

To probe the quaternary structure of the Ste2 receptor in living yeast cells (*S. cerevisiae*), we have implemented two-photon optical micro-spectroscopy[6,65] to acquire pixel-level fluorescence spectra of yeast cells expressing Ste2-GFP$_2$ and Ste2-YFP either singly or in combination with one another (see Materials and Methods). First, we obtained elementary emission spectra by imaging cells expressing only Ste2-GFP$_2$, which was used as a donor of energy (D), or only Ste2-YFP, used as an acceptor (A), and then normalizing the intensity spectra to their maximum intensity values.

Using the elementary spectra and a fitting algorithm described previously[66], we unmixed the composite fluorescence spectra obtained for individual image pixels for cells co-expressing Ste2-GFP_2 and Ste2-YFP. The unmixing procedure provided spatial intensity maps separately for the donor, k^{DA}, and the acceptor, k^{AD}, emission in the presence of each other (see Figures 1a and 1b). From such pairs of fluorescence maps, the apparent FRET efficiency, E_{app}, was calculated[6,72] for each image pixel (see Figure 1c).

Hand-drawn polygonal regions of interest (ROI) were made for each cell within either the k^{DA} or k^{AD} maps (whichever had a more clearly defined outline), and pixels belonging primarily to the cytoplasm were then removed from the maps using a computer algorithm that only retained a band ten-pixel wide within the ROI, as measured from the exterior of the ROI (see Supplementary Section SM2 for a full description of the method). This separation between intracellular and membrane receptors is facilitated by the inherent image-sectioning capabilities of two-photon microscopy. The resulting polygonal rings were subsequently divided into four segments using the computer program. The segmented ROIs were then transferred to the E_{app} maps (see Figure 1c for typical results), from which FRET efficiency histograms were generated (Figure 1d-f) by binning together the pixels with similar FRET efficiencies at a bin interval of 0.005. The E_{app} histograms from the randomly selected cell displayed in Figure 1 revealed varying levels of detail (i.e., locations along the E_{app} axis, amplitudes, and widths of the peaks in the histograms) that are often indicative of the presence of receptor oligomers, as previously described[27,29].

In order to determine the most probable quaternary structure of Ste2 oligomers in the absence and presence of the α-factor pheromone, we exploited the large number of cell-level histograms obtained in this study. Specifically, we extracted E_{app} values corresponding to two clearly visible peaks from each histogram (indicated by vertical red lines in Figure 1, panels d, e, and f) using an algorithm briefly described in the Materials and Methods section (with details given in the Supplementary Methods section SM4) and illustrated in Fig. S2. We used up to two peaks for each image segment to generate a histogram of peak positions, which is called a *meta-histogram*[6,7,29,66,73]. An E_{app} bin width of 0.02 was used to assemble the meta-histograms.

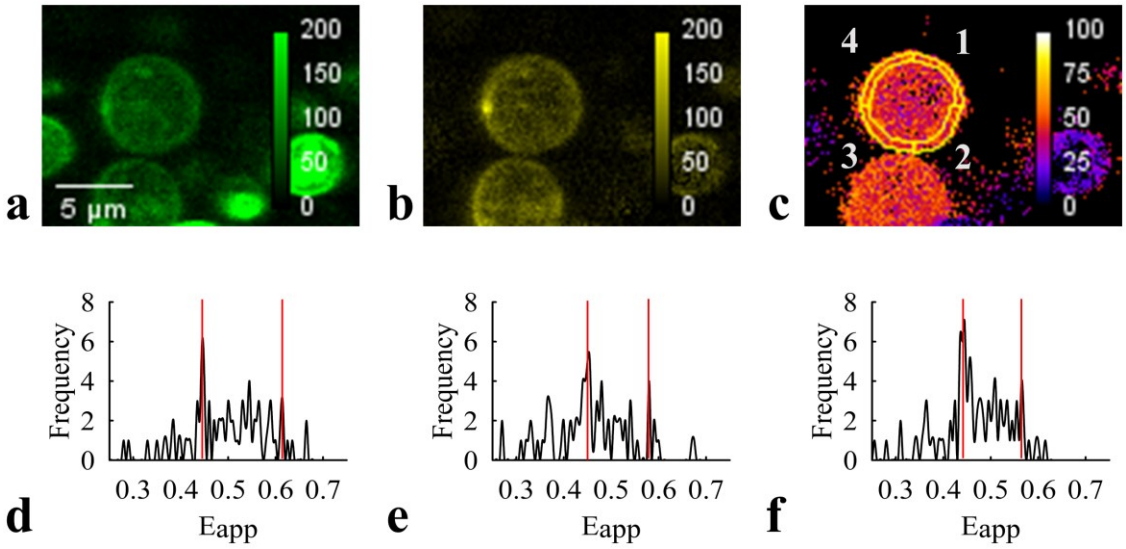

Figure 1. Typical results obtained from imaging yeast (*S. cerevisiae*) cells co-expressing Ste2-GFP$_2$ and Ste2-YFP. Spectral unmixing provided separate maps of the fluorescence signals of (a) donors in the presence of acceptors, k^{DA} and (b) acceptors in the presence of donors, k^{AD}. (c) Apparent FRET efficiency, E_{app}, maps were determined from the pixel-level values of k^{DA} and k^{AD}, as described in the Materials and Methods section. Contours defining regions of interest (ROI) were hand-drawn around the exterior of cells, and pixels were removed from the interior of the selections until a ring (with a width of ten pixels) encompassed only the plasma membrane; each such ROI was split into four segments as described in the Supplementary methods section SM2 and Fig. S2. Segmented ROIs were transferred to the E_{app} maps (shown as yellow curves in panel c), and histograms showing the number of pixels within a certain E_{app} bin range (Frequency) for different E_{app} values were generated from each segment using a bin size of 0.005 for E_{app}. Representative E_{app} histograms are shown in panels d, e, and f from segments 1, 3, and 4, respectively, whose average receptor concentrations were 131, 115, and 164 molecules/μm^2. The positions of the two most dominant peaks of these histograms (indicated with vertical red lines) were among the ones used to generate the meta-histograms shown in Figure 2, as described in the Materials and Methods (with more details given in section SM4) and illustrated in Fig. S2.

To determine average concentrations of receptors within each membrane segment, which was needed for sorting the segment-level E_{app} histograms used to assemble the meta-histograms, we first scanned the sample with 930-nm laser light (which provides good acceptor excitation) and then with 800-nm light (which only excited the donor). The 800-nm excitation was used to extract the apparent FRET efficiency (via Eq. (1) above), while both excitation wavelengths provide measured intensities used to estimate molecular concentrations of both the donors and acceptors[27,67] using Eqs. (4) and (5). Because photo-switching and/or photobleaching of the donor may occur more appreciably upon excitation at 800 nm, the order of excitation scans (i.e., first 930 nm and then 800 nm) was chosen to minimize donor photo-switching and/or photo-bleaching prior to determining acceptor concentration from fluorescence excited at 930 nm[74-76].

The total concentration of receptors per cell membrane area for each ROI segment was computed by adding the concentrations of donor-labeled and acceptor-labeled receptors (see Eq.

(6)) and converted, when necessary, into numbers of receptor molecules per image pixel using Eq. (7). The E_{app} histograms of each segment were then sorted in ascending order of the average receptor concentration per segment, regardless of which ROI (or cell) the segment originated from. As done previously[27], we selected only ROI segments with relatively low receptor expression levels in the assembly of E_{app} meta-histograms, in order to avoid the use of featureless histograms generated by mixing of multiple configurations of oligomers in pixels where the concentration of receptors is very high. We found that a good compromise between meta-histogram resolution and number of experimental data points occurred when choosing total receptor concentrations ranging from ~9 (corresponding to the lowest receptor expression level) to 203 molecules/μm^2 (with an average of 112 molecules/μm^2).

Examples of E_{app} meta-histograms obtained for two different ranges of receptor concentrations (i.e., 41 < molecules/μm^2 < 124 and 41 < molecules/μm^2 < 136) are shown in Figure 2a-d. For each concentration range, the meta-histograms were assembled by choosing either a single peak (panels a and c) or two peaks (panels b and d) per E_{app} histogram, for comparison. Peaks observed in meta-histograms have previously been ascribed to the FRET-productive configurations of the most probable receptor quaternary structure[27-29] and have been used to extract geometrical parameters corresponding to quaternary structure models[6,7,29,66,73]. The quaternary structure models predict a number of Gaussian peaks, whose relative positions (i.e., "means") are determined by only three parameters: the pairwise FRET efficiency, E_p, the ratio of the side lengths of the oligomer, r_1/r_2, and the acute angle between the sides, α (see Figure 2).

Inspired by our previous analyses involving Ste2[6,27], we first analyzed the current meta-histograms, corresponding to image segments from regions of the cells with low average receptor concentrations (i.e., ~9 to 203 receptors per μm^2), using a rhombus-shaped (i.e. r_1/r_2 = 1) tetramer model with an acute angle between sides of the rhombus of α = 60º. However, it has been determined that a parallelogram-shaped tetramer model better approximates the shape of the quaternary structure for a number of other GPCRs[7,29]. Therefore, aided by the large amount of high-quality data collected in this study, we wanted to refine the modeling of the Ste2 quaternary structure to see whether a more general parallelogram shape better approximates the structure of Ste2 as well. The parallelogram-shaped tetramer model allows for two opposite (or parallel) sides to be longer than the other two (i.e., $r_1/r_2 \neq 1$, see Figure 2i), which allows for the separation between the theoretical Gaussian peaks along the E_{app} axis of the meta-histogram to better match

the data and thereby revealing small changes in r_1 and r_2. More importantly, the difference between the two side lengths also causes the splitting of a single peak in the rhombus model into two peaks of the parallelogram mode (peaks 3 and 4 in Figure 2), as the corresponding donor-acceptor configurations (see Fig 2i) present different distances between their donors and acceptors in the r_1 and r_2 directions. This peak splitting adds exquisite precision to our determination of the two distances, as the difference between the positions of peaks 3 and 4 is directly related to the differences between the distances r_1 and r_2.

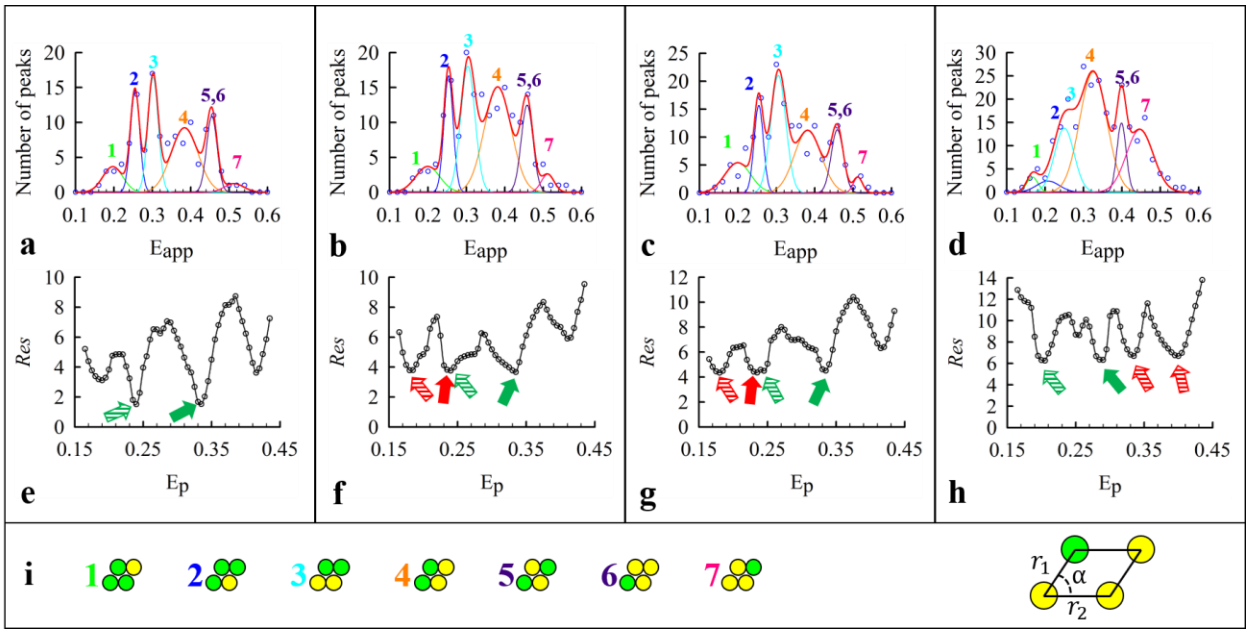

Figure 2. Typical meta-histograms obtained from yeast (*S. cerevisiae*) cells co-expressing Ste2-GFP$_2$ and Ste2-YFP in the absence of α-factor at low receptor concentrations, and their analysis using an appropriate quaternary structure model. Experimental meta-histograms (empty blue circles) obtained by collecting either single peaks (panels a and c) or two peaks (panels b and d) from each E_{app} histogram of the type shown in Figure 1 were fitted (solid red lines) using a reduced residual minimization algorithm (see section SM5 and panels e-h) to a general parallelogram-shaped tetramer model, which is comprised of seven Gaussian peaks corresponding to particular FRET-productive configurations of donors and acceptors within a tetramer (see panel i). The meta-histograms were assembled for two different receptor concentration ranges: 41 to 124 receptors/μm^2 (panels a and b) and 41 to 136 receptors/μm^2 (panels c and d). Positions of the seven meta-histogram peaks predicted by the model depend on only three parameters, E_p (pairwise FRET efficiency), r_1/r_2, and angle α (shown in i), which are used as adjustable parameters in the data fitting process. At the beginning of the fitting process, E_p was first set to 0.16, and the lowest possible reduced fitting residual (see Supplementary Methods section SM5) was obtained by adjusting the fitting parameters. The process was repeated several times after increasing E_p in a stepwise manner, and the reduced fitting residual vs. E_p was plotted (panels e-h). One such curve computed for each histogram is shown under its respective meta-histogram in the figure. The pair of complementary fits for each curve, indicated by two arrows with the same color, is obtained by simply switching between r_1 and r_2 values in the model. Since the two situations are structurally indistinguishable, only one of the fits (indicated by solid color arrows) is retained in our subsequent analysis. In addition, the *Res* vs. E_p plot may present two sets of such local minima, each set denoted by arrows of different colors. Usually, only one set of complementary fits provides the global minimum, but sometimes two such sets take similarly low *Res* values. Best-fit parameters and *Res* corresponding to the minimum indicated by the solid color arrow(s) were: E_p= 0.335, r_1/r_2 = 0.92, α = 65.88, and *Res* = 1.52 for panels (a) and (e); E_p= 0.240 and 0.335, r_1/r_2 = 0.94 and 0.93, α = 60.80 and 66.95, and *Res* =

3.75 and 3.66 for (b) and (f); E_p= 0.235 and 0.335, r_1/r_2 = 0.95 and 0.93, α = 59.29 and 66.91, and *Res* = 4.35 and 4.51, for (c) and (g); E_p= 0.290, r_1/r_2 = 0.92, α = 66.75, and *Res* = 6.32 for (d) and (h).

In addition to the model-predicted peak positions, the theoretical curves also include the amplitudes of the individual Gaussians, which depend directly on the frequencies of occurrence of each FRET-productive configuration[6,28], as well as the widths of the Gaussians, which depend on the angles between the transition dipoles of each fluorescent tag and the degree of cylindrical averaging caused by rotational diffusion of the tags attached with linkers to these membrane proteins[6,77,78]. Analysis of amplitudes may reveal proportions of different oligomer sizes (such as dimers and tetramers) as well as proportions of donor-only to donor-acceptor oligomers, which we have described in previous work involving this or other receptors[7,27,29]. At the same time, the Gaussian widths mostly limit the accuracy of the acute angle α, which is not the main focus of this work, and the visibility of the peaks, which is enhanced via the meta-histogram approach described above, although they might also affect the accuracy of the distances between tags. In this latter regard, the distances shown in this paper should be regarded as relative (to one another). Therefore, neither of these additional Gaussian-related parameters is included in our theoretical model at this time, as they would add unnecessary complexity to our analysis, which is strictly focused on identifying geometrical substates within one of the dominant oligomeric species for this receptor (i.e., the tetramer)[27].

To extract the needed information from the meta-histograms, the Gaussian amplitudes, standard deviations, and the parameters determining the Gaussian peak positions were adjusted systematically for each model used, in order to minimize the reduced fitting residual, i.e., the sum of the squared differences between experimental and theoretically predicted data points (i.e., the usual fitting residual) divided by the number of degrees of freedom, as expressed by Eq. (S6) of the Supplementary Methods Section SM5. The number of degrees of freedom of the data is the number of data points minus the number of fitting parameters corresponding to each model. The reduced fitting residual was needed to properly compare the two models, due to the fact that the general parallelogram model has more fitting parameters than the rhombus tetramer model (r_1/r_2 = 1 and α = 60º were held fixed for the rhombus model as stated above). The reduced residual weighs the gain in the goodness of fit (encapsulated in the fitting residual), brought about by the flexibility provided by additional fitting parameters, against the penalty that should be paid (i.e., a decrease in the number of degrees of freedom) for increased model complexity.

As seen in Supplementary Figure S4, the general parallelogram-shaped tetramer model fitted the data significantly better than did the rhombus tetramer model, with vastly lower values for the reduced fitting residuals: 1.735 for parallelogram vs. 6.380 for rhombus in absence of ligand, and 1.243 for parallelogram vs. 7.712 for rhombus in the presence of ligand. While the deviations of the quaternary structure model of Ste2 from that of a rhombus revealed by this preliminary analysis were relatively small (i.e., less than 10% difference between the lengths of the two sides of the parallelogram, with the angle between them just a few degrees larger than 60º), being able to capture them with such exquisite precision allows us to ask more detailed questions regarding the possible effect of ligand binding on the geometry of the oligomer. This ability to extract small differences in the quaternary structure of Ste2 performed in the present study is due to several modifications to the method as discussed in the introduction. Furthermore, our current ability to automatically separate membrane regions within the images into smaller segments allowed the capture of local fluctuations in FRET efficiencies and permitted generation of larger pools of data (>10,000 histograms/experiment) for dramatically improved statistics. For typical results pertaining to samples treated with the α-factor ligand and analyzed in a similar manner as shown in Figure 2, see Supplementary Figure S5.

Based on the results of this preliminary analysis, we decided to apply the parallelogram model to the analysis of all the meta-histograms going forward.

3.2 Computer simulations reveal the effect of noise on meta-histograms

One of the first questions that may arise while glancing at the meta-histograms of the types displayed in Figure 2 concerns the extent to which noise affects the visibility of the various peaks, and the ability to extract oligomer geometrical information from their number and location. To address this potential concern, we have conducted computer-based numerical simulations at the level of single oligomeric complexes per pixel, with an aim to replicate conditions leading to experimental meta-histograms (see Supplementary Methods sections SM8 and SM9 for a detailed description of the simulations). For simplicity, in these simulations we opted to use the rhombus-shaped tetramer model for the oligomeric complex to be simulated. Using E_p = 0.20, α = 60º, and r_1/r_2 = 1, we calculated the theoretical E_{app} peak positions, along with the expected donor and acceptor intensity levels, for all configurations of the rhombus. Using the expected donor and acceptor intensities for a given configuration, we created normal probability distributions, defined

by Eq. (S23), which were centered at the expected intensity values of each. The width of the normal probability distribution was determined from a fixed signal-to-noise ratio (SNR), according to Eq. (S24). For each pixel in a simulation, a random intensity value for both the donor and acceptor was chosen from the corresponding probability distribution which was constructed for the particular oligomer configuration found in said pixel, and a value of E_{app} was then calculated by plugging the two randomly chosen intensity values into Eq. (1). E_{app} histograms were constructed from a collection of 1000 pixels, and a meta-histogram generated from 500 E_{app} histograms, using the same protocol described in section 2.3. Since the signal level in all simulations was fixed to intensity values which correspond to a single tetramer for each simulated pixel, we could generate meta-histograms for a wide range of signal-to-noise ratios (*SNR*) simply by changing the width of the normal probability distributions constructed using Eq. (S23).

Although a naïve prediction would be that noise may generate artificial peaks in the meta-histograms, our simulations showed that addition of large amounts of noise generated no additional peaks. For very low values of *SNR* (≤ 1), the meta-histograms did contain a smooth broad background distribution across all E_{app} values which was centered around E_{app} = 0.5 (see Supplementary Figures S9 and S10). However, within these histograms generated for $SNR \leq 1$, individual peaks, while relatively small, are still clearly visible, and their locations corresponded to the FRET values of the various tetramer configurations in the simulation. The range of *SNR* levels corresponding to live-cell experiments were determined based on a comparison of live-cell intensity measurements to those from a control experiment involving characterization of EMCCD noise for various light intensity levels (see Supplementary Methods section SM9). The simulated meta-histograms with *SNR* levels corresponding to our live-cell experiments, i.e., $20 \leq SNR \leq 30$ on average, are indicated in Supplementary Figures S9 and S10 with red boxes. Thus, from our simulated meta-histograms, we can safely assume that noise does not generate artificial peaks in the experimental meta-histograms and that in fact the challenge is to reduce the noise such that the peaks are not smeared or even obliterated.

Note that, although based on these simulations we could select an arbitrary number of peaks from each histogram for assembling the meta-histogram (in order to better resolve the quaternary structure substates), we noticed that experimentally only one out of twenty image segments showed three peaks in their E_{app} histograms. Other peaks were either washed out by noise, or they were entirely absent since a single image segment can only comprise a limited number of donor-

acceptor combinations that generate those peaks. Therefore, for uniformity and, more importantly, as an additional filter used to reduce experimental meta-histogram smearing, we placed an upper limit of two on the number of peaks.

3.3. Contributions of incomplete labeling and photobleaching to the meta-histograms

It is known that maturation of the fluorescent tags takes time and therefore some 20% of the total fluorescent protein content of the cell may not be actually fluorescent[79]. Although most fluorescent tags are expected to fully mature by the time the labeled Ste2 passes quality control and is delivered to the cell membrane, some might remain non-fluorescent, as the protein synthesis and sorting machinery is oblivious to biochemical formation of the chromophore inside the fluorescent protein barrel. In addition, it is known that there is always a fraction of fluorescent proteins in a dark state at acidic pH. Furthermore, photobleaching of the already mature proteins by laser light during imaging[80,81] may also appear as incomplete labeling. Any such non-fluorescent tags would inadvertently create the appearance of oligomers (or combinations of donors and acceptors) with different sizes, such as monomers, dimers, and trimers, in addition to the tetrameric configurations presented in Fig. 2i (S3, S4e, and S5i) and Supplementary Table S1.

The E_{app} histogram peaks corresponding to these artefactual oligomers fall into two categories: Those that overlap with the tetramer peaks (cf. the mathematical expressions in Supplementary Table S1), and those that do not overlap and thus contribute to the smearing of the meta-histograms. The first category is of no concern, as they can only alter the amplitudes of the tetramer peaks but not their positions along the E_{app} axis. The second category would only contribute to histogram smoothing (similar to the effect of random noise explored in the previous sub-section), given their multiplicity and that their frequencies are significantly lower than those of the tetramer (since most molecules are actually fluorescent), and therefore could not obscure the histogram peaks originating from the fully labeled tetramers, which are the dominant ones. The information carried by the dominant peaks corresponding to the structure of interest is further distilled through our use of the meta-histogram approach (see above and Ref[28]), which is virtually the same as discussed in section 3.2 and illustrated in Figures S8 and S9.

3.4 Detailed meta-histogram analysis reveals multiple oligomeric conformation sub-states

We employed an iterative process for fitting the meta-histograms with the parallelogram shaped tetramer model. In this fitting procedure, one parameter, E_p, was fixed at a particular value, and all

other parameters were adjusted until the reduced fitting residual, *Res*, was minimized. Then the value of E_p was increased by a small increment, and the fitting procedure involving all other parameters run again. This iterative fitting procedure was repeated for a range of E_p values ($0.16 \leq E_p \leq 0.5$), and the minimum *Res* value obtained for each E_p value was plotted against its corresponding E_p value; examples of *Res* vs. E_p plots are shown in Figures 2e-h. Note that there is in fact a pair of complementary fits for each curve, indicated by two arrows with the same color, and which correspond to simply swapping the value of r_1 and r_2 in the theoretical model. Since switching between r_1 and r_2 results in two oligomers that are structurally indistinguishable, only one of the minima (indicated by solid color arrows in Fig. 2) is retained in our subsequent analysis. The corresponding complementary fit to a minimum which is retained in subsequent analysis is indicated in Fig. 2 by a striped arrow of the same color.

As seen in Figure 2, fitting the E_{app} meta-histograms with a mathematical expression generated from the parallelogram-shaped tetramer for a range of E_p values reveals one global minimum and possibly a second, local, minimum in the plots of *Res* vs. E_p (after excluding complementary minima corresponding to swapping between r_1 and r_2 values). For example, for the meta-histogram shown in panel a (assembled from single histogram peaks with concentrations of 41 receptors/μm^2 to 124 receptors/μm^2), the fitting residual reached a global minimum (indicated by the solid arrow in panel e) for a pairwise FRET efficiency E_p= 0.335. As we added comparatively few peaks, extracted from a pool of histograms corresponding to receptor concentrations of 124 receptors/μm^2 to 136 receptors/μm^2, to the original meta-histogram in panel a to generate the meta-histogram shown in panel c, the *Res* developed two nearly equal minima (indicated by solid arrows in panel g) corresponding to two different sets of values for E_p and the other fitting parameters. We took this as evidence that there must exist more than one quaternary structure sub-state for Ste2 oligomers, each characterized by its own set of best-fit E_p, r_1, r_2, and α values. In other words, a set of segment-level histogram peaks may generate a meta-histogram in which one quaternary structure sub-state dominates, while for a slightly different set of peaks used to generate a meta-histogram, another sub-state may dominate or two substates may become equally probable, just by pure chance and not because the upper limit in concentrations increased slightly. (Note that the concentrations could only potentially change the number of protomers within an oligomer but not the oligomer geometry, which is how we describe quaternary sub-states.) The same conclusion may be reached by comparing the data in panels b and d and, indeed,

by comparing any two meta-histograms generated from a completely different set of histogram peaks.

To investigate this hypothesis systematically, we first took all 2,332 (ligand, absent) and 2,370 (ligand, present) histogram peaks obtained from segments with receptor concentrations less than 203 molecules/μm^2, separated them into groups based on the experimental day they were acquired, and then listed each group in ascending order of their total receptor concentration. We then created E_{app} meta-histograms for each experimental day using the first 100 histogram peaks in the sorted list (i.e. peaks which originated from the segments with the lowest concentration values). These initial meta-histograms were then analyzed using the iterative fitting procedure described above and illustrated in Figure 2. Next, we created additional meta-histograms by adding peaks, typically in increments of 50, to the existing ones. This process of building up meta-histograms incrementally was repeated until the meta-histograms for a particular experimental day contained peaks from a maximum of 300 different segments; the highest concentration of a segment used in any of the constructed meta-histograms was 203 receptors/μm^2. In special cases where we noticed a switch from a single minimum to two minima along the *Res* vs. E_p curves, e.g., as shown in Figure 2e-h, we occasionally introduced a smaller increment of 25 peaks in an attempt to capture both minima. When the *Res* values corresponding to two such local minima were nearly equal, we used both sets of corresponding best-fit parameter values in our subsequent analysis (described below).

Meta-histograms were analyzed using the iterative fitting procedure for each incremental step in the number of peaks; a total of 65 meta-histograms were constructed and analyzed for data obtained in the absence of ligand, and 62 in the presence of ligand. From the different sets of best-fit E_p and r_1/r_2 values obtained for the quaternary structure in the absence and presence of α-factor ligand, the two parallelogram side lengths were computed using the expression $r = R_0\left(1/E_p - 1\right)^{1/6}$. In this regard, the previously published value of the Förster radius for the GFP$_2$/YFP pair, R_0= 57 Å[59], serves as a "molecular ruler"[82]. The 65 sets of r_1 and r_2 distances thus obtained in the absence of ligand and 62 in the presence of ligand were used to generate separate histograms (referred to as r_1 or r_2 distance histograms) for the frequency of occurrence of r_1 and r_2 distances (see open black circles in Figure 3). At this exquisite (sub-Ångstrom) resolution, one can clearly distinguish two or three peaks in the distributions of distances, indicating the presence

of multiple quaternary conformation sub-states (see Discussion section below for elaboration on this point).

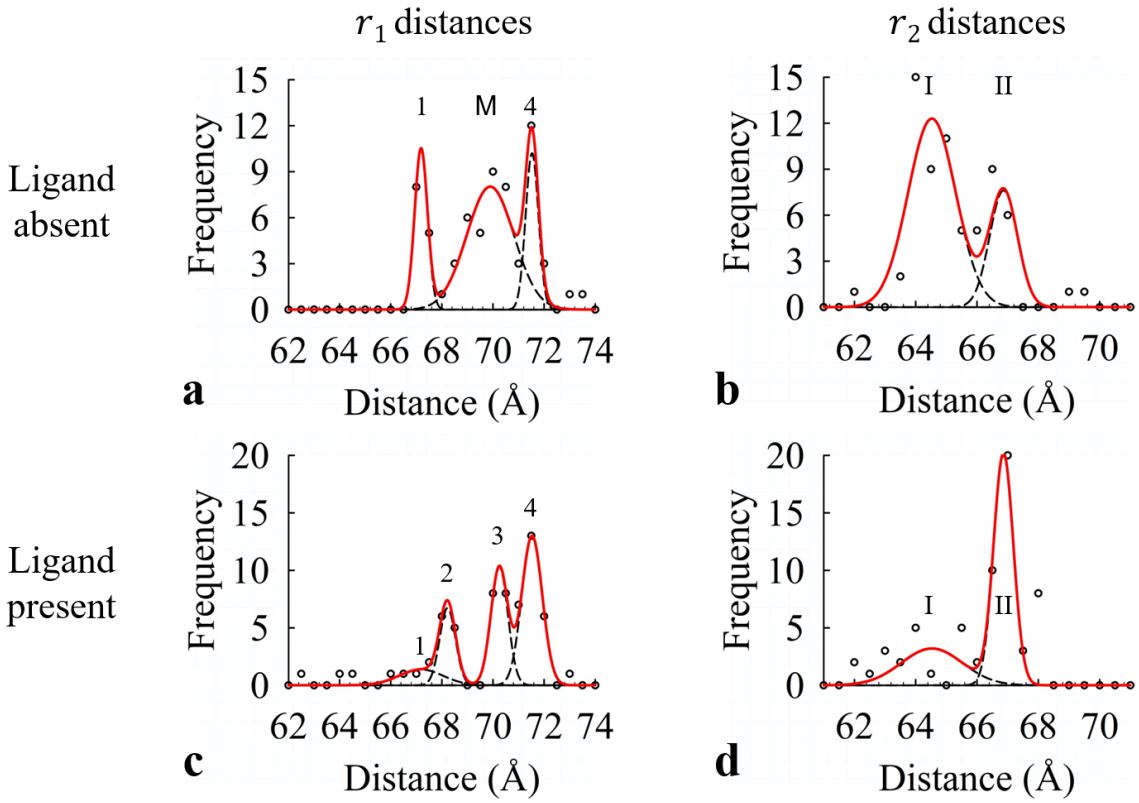

Figure 3. Histograms of frequencies of occurrence of the side lengths of the general parallelogram-shaped tetramer obtained from fitting the theoretical model (Figure 2i) to the experimental meta-histograms. (a) The r_1 distance values (black circles) obtained in the absence of α-factor were binned into 0.5 Å bins and fit with a model consisting of a sum of three Gaussian functions (dashed black lines) corresponding to three different conformational states. The Gaussian parameters were adjusted to minimize the Res between the fitted model curve (solid red line) and the experimental data points. (b) Similarly, the r_2 distance values in the absence of α-factor were used to generate a histogram (with 0.5 Å bin size) which was fit with a sum of Gaussian curves corresponding to two conformational states found for this distance. The same protocol described for panel a was used to minimize the reduced χ^2 between the fitted curve and the experimental points. (c) Histograms for r_1 distance values obtained in the presence of ligand and fit with a sum of four Gaussians. (d) Histograms for r_2 distance values obtained in the presence of ligand and fit with a sum of two Gaussians. Plots in panels a and b each contain 65 data points, while those in panels c and d contain 62 data points (corresponding to as many meta-histograms of FRET efficiencies). The best-fit parameter values of each of the Gaussians used to fit the distance histograms are listed in Tables 1 and 2.

The positions of the different peaks in the r_1 and r_2 histograms were determined by fitting a sum of Gaussian functions (represented by solid red lines in all panels of Figure 3) to the experimental data points (shown as empty circles). Since some of the peaks (labeled by "1" and "4," in the r_1 histogram and by "I" and "II" in the r_2 histogram) were visible in both the presence and absence of ligand (albeit with different amplitudes), the fitting required that the mean positions of those Gaussian functions were held fixed relative to one another during the process (i.e., simultaneously fit). However, when comparing the distributions of the r_1 data for ligand treated vs. ligand absent, the peaks located between peaks 1 and 4 do not align in a similar fashion. Therefore, a single Gaussian function was used to fit the middle peak of the r_1 histogram (labeled by "M" for mixture) in the absence of ligand, whereas two separate Gaussian functions were used to fit the peaks labeled "2" and "3" in the r_1 histogram obtained in the presence of ligand.

Table 1. Best-fit parameters for the multiple Gaussian curves used to model the r_1 distances found for the various conformational states of the parallelogram-shaped tetramer for Ste2 shown in Figures 3a and 3c.[1]

Ligand	Parameter	Peak 1	Peak 2	Peak M	Peak 3	Peak 4
Absent	Mean (Å)	67.2	−	69.9	−	71.5
	Amplitude	10.4	−	8.0	−	10.2
	Standard Deviation (Å)	0.3	−	0.9	−	0.3
Present	Mean (Å)	67.2	68.2	−	70.3	71.5
	Amplitude	1.4	6.7	−	10.3	13.0
	Standard Deviation (Å)	0.9	0.3	−	0.3	0.4

[1] The best fit for the ligand absent (model consisting of three peaks) and ligand present (model consisting of four peaks) histograms had a reduced Res of 0.71 and 0.30, respectively.

Table 2. Best-fit parameters for two Gaussians used to model the distributions of r_2 distances found for the conformational states of the parallelogram-shaped tetramer for Ste2 shown in Figures 3b and 3d.[2]

Ligand	Parameter	Peak I	Peak II
Absent	Mean (Å)	64.5	66.9
	Amplitude	12.3	7.6
	Standard Deviation (Å)	0.8	0.5
Present	Mean (Å)	64.5	66.9
	Amplitude	3.2	20.0
	Standard Deviation (Å)	1.0	0.3

From the fitting of the r_1 distance histogram in the presence of α-factor, we can identify the two middle peaks in Figure 3c (i.e., peak 2 and 3) as intermediate conformational states between the two fixed peaks (i.e., peak 1 and 4) since they do not exist in the absence of α-factor. As is clearly seen in Figures 3b and d, the relative amplitude of peaks I and II of the r_2 distance histograms change when ligand is added, with the peak II amplitude increasing and, thereby, the peak I amplitude decreasing. To quantify such changes in the relative abundance of all the distance histogram peaks when ligand was added, we calculated the relative percentage fraction for each peak by evaluating the area under each Gaussian function and then dividing each by the sum of the areas under all Gaussians used in the model (see Figure 4).

[2] The best fit for the ligand absent and ligand present histograms had a reduced Res of 3.53 and 4.60, respectively. The histograms were simultaneously fit using equivalent mean positions of the two individual Gaussian curves.

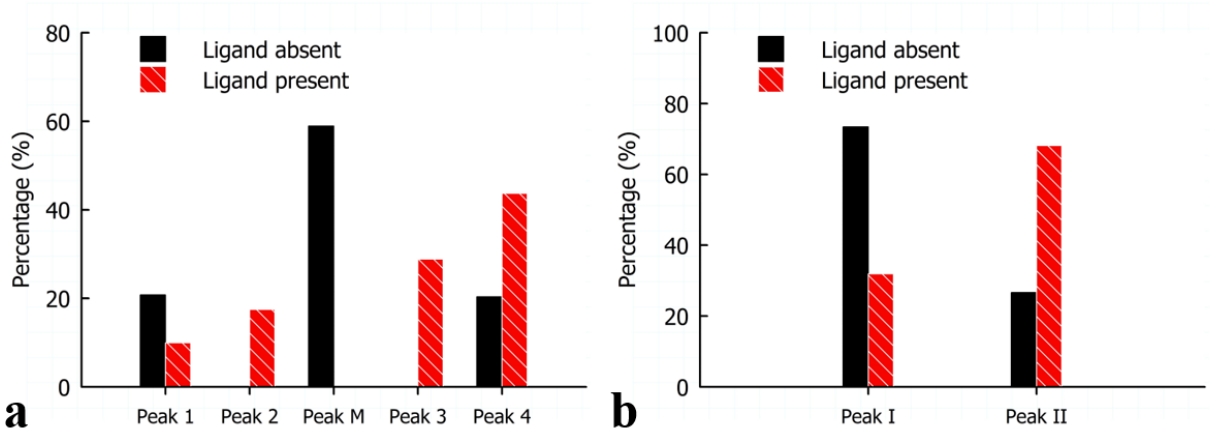

Figure 4. Relative abundance of the conformational states for r_1 and r_2 distances of the parallelogram-shaped tetramer formed by Ste2 in the absence and presence of α-factor. (a) To compute percentage (%), the area under each Gaussian used to fit the r_1 distance histograms shown in Figure 3a and 3c is divided by the total area under the curve of their respective models (i.e., the sum of the Gaussian curves comprising the model). In the absence of α-factor (black bars), three Gaussian curves (or "peaks") are required to best describe the data (labeled here as peak 1, M, and 4), while in the presence of α-factor, four distinct peaks occur (described by peaks 1, 2, 3, 4). The percentage (%), or relative abundance, of each peak within a specified model shows which states are more favored in each scenario. (b) Similarly, the relative abundance of each Gaussian curve used to model the r_2 distance histograms of Figure 3b and 3d were computed using the protocol described in panel a, in both the absence and presence of α-factor (black and red bars, respectively). Here, the model is comprised of two Gaussian curves (I and II), for which the bar heights show a major shift from absence to presence of α-factor, indicating preference of conformational states under each scenario.

The bar chart of the relative abundance of r_1 distance values presented in Figure 4a shows that in the absence of ligand, peak M (r_1=69.9 Å) dominates the distribution, but when ligand is present peaks 2 (r_1=68.2 Å) and 3 (r_1=70.3 Å) are closer in amplitude (17% and 28%, respectively) with peak M disappearing entirely. Peak 1 (r_1=67.2 Å) decreased while peak 4 (71.5 Å) increased, making the longer r_1 distances more probable than the shorter ones in the presence of ligand (see amplitudes and standard deviation values in Table 1). Similarly, the relative abundance of r_2 distance values (Figure 4b) changed more markedly after ligand was added, with the peak corresponding to a longer r_2 distance increasing appreciably. Specifically, Peak I (r_2=64.5 Å) became significantly less abundant than peak II (r_2=66.9 Å) in the presence of ligand, indicating a significant propensity of the structure to assume conformations with longer distances between the

fluorescent tags of the protomers (i.e., 66.4 Å$\leq r_2 \leq$ 67.4 Å; see amplitudes and standard deviations in Table 2).

We note in passing that, unlike the histograms for r_1 and r_2, the histograms for the acute angle α (defined in Fig. 2i) did not unambiguously reveal peaks that maintained the same position in the presence and absence of ligand, with the exception of a peak positioned around 63° (see Supplementary Figure S12). In addition, the distribution of values of α became significantly narrower (with the 63° peak becoming higher) after addition of ligand, consistent with the notion that the receptor is constrained to occupy certain stable quaternary states by the interaction with the ligand. More detailed analysis of the angle distribution would require higher angular resolution than available at this time.

4. DISCUSSION

Conformational changes in the tertiary structure of GPCRs during the activation process has been heavily investigated in recent years. Early hypotheses regarding possible GPCR tertiary structures depicted the receptor as a simple switch which existed in either an inactive or active state. However, a growing body of evidence suggests that activation of GPCRs is not a binary operation, but rather that the tertiary structure conformation can exist in a series of intermediate states[54], with a range of activity levels possible across the distribution of conformations as shown by fluorescence-based techniques[30,83], FNMR[32], AFM[84], electron microscopy[85], X-ray crystallographic studies[38], and theoretical simulations using crystal structures[2,33,86,87]. From crystal structure studies of individual GPCRs, it has been observed that the intracellular region of TM1, TM3, TM5, TM6, and TM7 move outward from one another when ligand is bound[2], with TM6 showing the most pronounced outward movement in the cytoplasmic end of the helix as compared to its membrane-integrated portion, and TM5 showing helical extension[38,87].

The purpose of our study was to investigate the quaternary structure organization of the Ste2 receptor, with particular emphasis on what effect, if any, ligand binding has on this structure. As it will be discussed in more detail below, the results presented in Section 3 strongly indicate that not only the tertiary structure of individual GPCR protomers within a protein complex but also the quaternary structure may exist in multiple sub-states; in fact, there must be a causal relationship between the two, as hinged motions of transmembrane domains belonging to abutting protomers may result in changes in the distance between the center of mass of the protomers.

To help visualize the likelihood of Ste2 to be in a particular quaternary structure substate in the presence and absence of ligand binding, we have drawn theoretical potential energy landscapes[30,32,33,54,83] depicting the basal and active conformations of the oligomer, as seen in Figure 5. Potential energy landscapes, which have been extensively used as a convenient visual tool for discussing protein conformations, represent the energy of the quaternary conformations along the receptor activation pathway[30,32,33,54,83]. Conformational states with lower energy are more stable, and thus are more likely to be populated. These stable conformations are represented by potential wells, or minima, in the energy landscape. The number and depth of such wells illustrated in Figure 5 were informed by analysis of the r_1 and r_2 histograms in Figure 3 and relative abundance plots in Figure 4. Specifically, a high relative abundance of a particular stable quaternary conformational sub-state corresponds to a deeper well in the potential energy landscape, while high probability of transition from one state to another is represented by a higher energy barrier between them.

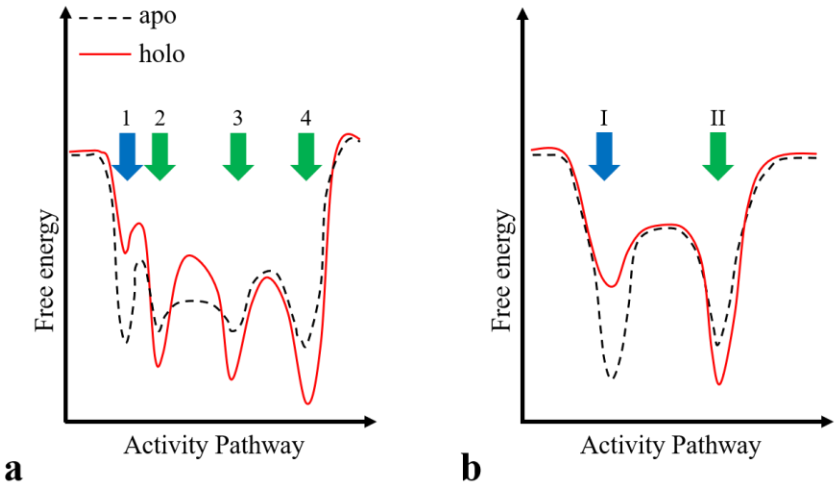

Figure 5. Schematic representation, using free energy landscape diagrams, of the multiple conformational states of the Ste2 quaternary structure in absence and presence of α-factor pheromone corresponding to the r_1 (a) and r_2 (b) distances between protomers within an oligomer. The schematics were drawn based on the distributions of the r_1 and r_2 side lengths of the parallelogram representing the Ste2 oligomer shown in Figure 3 and their relative abundance presented in Figure 4. The r_1 distribution obtained in the absence of ligand shows how none of the four states is more probable than the next, and the barrier between active state 2 and active state 3 is lower than the barrier between other states, making these states more unstable than the inactive basal state 1 and active state 4. When ligand is present (solid red curve), state 1 diminishes while the probability of the receptor residing in the higher activity states (2, 3, 4) increases, as reflected by the lowering of energy minima upon binding of ligand. For the free energy diagram corresponding to r_2 distances, both the inactive (I) and active (II) conformations are present in abundance in the

absence of ligand, with a slight preference for the inactive state. When ligand is administered and bound to receptors within the oligomer, the active conformation dominates.

Two significant observations may be made with regard to the effect of ligand on the probability associated with the occupancy of each quaternary conformation. Firstly, we see from Figure 4 that treatment of Ste2 with α-factor altered the relative abundance of each of the quaternary conformational states when compared to the conformations of Ste2 in the absence of ligand except for peaks 2, 3, and M in Figure 4a. Secondly, inspection of the r_1 distance histograms suggests that the Ste2 quaternary structure can quickly oscillate between multiple quaternary conformational substates.

With regard to the first observation, we note that the relative abundance of the shortest r_1 and r_2 distances (peaks labeled by 1 and I in Fig. 4) both decreased appreciably when ligand was administered. Conversely, the abundances of the states characterized by longer r_1 and r_2 distances (peaks labeled by 4 and II in Fig. 4) both increased upon addition of ligand. From this, we ascertain that the activity of the Ste2 complex, which is presumed to be higher in the presence of ligand, increases along with the interprotomeric distances of the quaternary structure. Therefore, the potential energy wells corresponding to the tighter conformation (i.e., shortest r_1 and r_2 distances) are drawn to the far left of the energy landscape diagram in Figure 5 (indicated by the solid blue arrows); the change in relative abundance of this inactive basal state conformation upon ligand binding is depicted in Figure 5a and b as a decrease in the depth of the energy well attributed to this inactive state. Likewise, we attribute the two longest r_1 and r_2 distances to those of the fully active conformation and draw the associated energy wells to the far right of the potential energy landscape of Figure 5. We find not only that the interprotomeric distances of the Ste2 quaternary structure increase as the receptor switches from the basal state to the fully active state, but also that such increase does not scale equally in both dimensions. We see from a comparison of the r_1 and r_2 distances listed in Tables 1 and 2 that the change in distances between protomers occurring along one dimension of the parallelogram (r_1 distance) is more pronounced than the change occurring along the other (r_2 distance). If the adjustment of the position/orientation of the TM domains in individual Ste2 protomers is such that the specific TMs which serve as binding interfaces between protomers along r_1 flare out more than those TMs involved in the binding interfaces between protomers separated by r_2, then one could explain why elongation was more

pronounced along one dimension of the tetramer versus the other (see Supplementary Figures S3 and S7).

The second significant observation mentioned above, that the Ste2 quaternary structure can quickly oscillate between multiple quaternary conformational substates, is supported by the fact that the extremely broad peak seen in Figure 3a (labeled Peak M) separated into two well defined narrow peaks when Ste2 was exposed to ligand (labeled Peak 2 and 3 in Figure 3c). Following our hypothesis that Peaks 1 and 4 correspond to inactive and fully active states, respectively, we attribute the peaks located between Peak 1 and 4 to semi-stable partially active conformational states. This broad peak (Peak M) is likely due to the protein complex shuttling between two partially active intermediate conformations which are separated by a low, flat energy barrier. Our interpretation of this situation is represented by the dashed black line in Figure 5a, which shows a low energy barrier between the two energy minima identified as states 2 and 3. The receptor complex can populate these conformational substates even in the absence of ligand, as is evident from the high relative abundance value calculated for Peak M in Table 1. However, because of the low energy barrier between these intermediate states, thermal perturbations would allow the quaternary structure to sample a multitude of configurations between the two states (i.e., Peaks 2 and 3) on a time scale which is faster than can be captured using our instrument. Only when ligand is added are these states "locked in" for long enough time to be captured via FRET spectrometry, an effect which both deepens the minimum and increases the height of the barrier between the two partially active states[54]. A similar phenomenon of partially active states being populated in the absence of ligand has been observed in the adrenergic 2A receptor, where four conformational states (two inactive and two active) were always present[32]. Agonist binding simply shifted the equilibrium of the conformations, with the higher activity states becoming more populated upon ligand binding.

One potential explanation as to why the Ste2 quaternary structure samples multiple intermediate states in the presence of ligand may be a result of sequential ligand binding (multiple step binding process), which has been shown to occur for other GPCRs[31]. Sequential ligand binding occurs when the contacts between the receptor and ligand do not form at the same time. Each contact which is formed between receptor and agonist results in a different conformational intermediate of the receptor, with the receptor becoming more active with each added contact. A recent study using atomic three-dimensional homology-based simulations showing Ste2 ligand

binding occurs between 26 residues primarily within transmembrane helices H1, H5, and H6 which may suggest that the three states identified as 2, 3 and 4 in Figure 3c and Figure 5a might actually be a result of sequential binding of the agonist to one of each of these helices (in an order which is currently unknown[88]). Each new contact which is made between the ligand and a particular helix would result in a conformational change of the Ste2 receptor, and hence induce a change in the quaternary structure as well. Another GPCR, the β_2 adrenoceptor, shows that upon each sequential step of agonist binding, some stabilizing intramolecular interactions are broken which allow for a higher probability that additional contacts may form as the receptor explores its conformational landscape[31]. The plasticity of intramolecular interactions (i.e., changes of distances between TMs, or forming new bonds/breaking previously formed bonds) as a GPCR binds at multiple steps with an agonist may provide further evidence of multiple activity levels within the tertiary structure, which is a concept we draw upon to describe similar effects at the quaternary level.

An alternative explanation for the existence of multiple quaternary substates may lie in the concept of membrane potential depolarization. Previous studies have shown that the muscarinic receptor type 2 (M2) displayed tertiary conformational changes which were induced by changes in membrane potential, particularly in the ligand-binding pocket, leading to a number of conformational states[89,90]. By similarity, the muscarinic receptor type 1 (M1) was assumed to bind agonist for a depolarized membrane which resulted in an acceleration of the transition from a quiescent to an active conformation, assuming multiple states along the path of activation[91]. It is therefore reasonable to assume that the existence of multiple inactive and active states (including partially active substates) at the tertiary level may be reflected at the quaternary level.

One potential effect that may perhaps be ruled out as the cause of Ste2 existing in multiple conformational substates relates to the preassembly of G-proteins and their pre-coupling with GPCRs, namely the possibility that different numbers of G-proteins are pre-bound to the GPCR. Li et al.[92] showed that preassembly of the heterotrimeric G-protein is highly independent of ligand presence and that the Gα-subunit alone is found in low abundance and is unlikely to bind to receptors at a basal level. Their findings also suggest that a basal level of preassembled Gαβγ bound to receptors in the absence of ligand is much lower compared to when it is present.

5. CONCLUSIONS

While the findings presented in this work remain consistent with the previous finding that Ste2 forms parallelogram-shaped tetramers at relatively low concentrations within the plasma membrane, the more elaborate set of experiments, larger sample size, and improved methodology resulted in the unprecedented experimental detection of Ste2 quaternary structure substates in living cells. We also found that, when Ste2 was exposed to agonist ligand, the inter-protomeric distances increased, suggesting a quaternary structure conformation that corresponds to the receptors being in a more active state.

The work presented here demonstrates the power of FRET spectrometry to detect shifts in the abundance of specific quaternary conformational states upon the binding of an agonist. While unambiguous interpretation of the nature of all the states identified in our work (e.g., states 2 and 3) would require additional experiments performed in the presence of different ligands (such as agonists, partial agonists, inverse agonists, and antagonists) as well as G proteins, the available literature (cited above) corroborates our observations that such states exist and that they can be modulated by ligand binding. The present methodology may be, of course, used in the future to study dynamic behavior of the quaternary structure of any GPCR. Furthermore, by combining FRET spectrometry with the complete atomic crystal structure of the GPCR under study, information which is currently lacking for the Ste2 receptor, the binding interfaces and binding energies between protomers within the oligomer could be ascertained[28]. Availability of crystal structure information would also facilitate identification of a more direct connection between the hinging motion of the receptor transmembrane domains and the receptor quaternary structure, which would allow probing the former by monitoring changes in the latter in the absence and presence of various ligands.

SUPPORTING INFORMATION

The Supporting Information is available free of charge.

- Detailed descriptions of select aspects of the methods which are not elaborated upon within the main body, including: thresholding pixel level fluorescence intensities on donor/acceptor spatial intensity maps (Section SM1), automated membrane isolation and segmentation in spatial intensity maps (Section SM2), segment filtering using goodness-of-fit criterion (Section SM3), automated E_{app} histogram peak selection routine (Section SM4), fitting of meta-histograms using quaternary structure models (Section SM5), testing

the uniqueness of meta-histogram fittings (Section SM6), determination of receptor concentration for membrane cross-sections (Section SM7), investigation of the impact of noise on meta-histograms using simulations (Section SM8), characterization of EMCCD camera noise for various signal levels (Section SM9)

- Figures providing additional data and analysis along with depictions of methods, including: isolation and segmentation of cell membrane micro-photographs (Figure S1), E_{app} histogram peak selection routine (Figure S2), geometrical model of a general parallelogram-shaped tetramer oligomer (Figure S3), comparison of meta-histogram fitting results using rhombus-shaped and general parallelogram-shaped tetramer models (Figure S4), meta-histograms obtained from cells exposed to α-factor (Figure S5), testing uniqueness of meta-histogram fit (Figure S6), schematic diagram representation of Ste2 receptor conformational substates (Figure S7), computer-simulated E_{app} histograms (Figure S8), meta-histograms constructed from computer-simulated E_{app} histograms generated for various signal-to-noise ratios (Figures S9 and S10), characterization of EM-CCD camera noise for various signal levels (Figure S11), histograms of the frequency of occurrence of the acute angle α of the general parallelogram-shaped tetramer model (Figure S12), representative parallelogram tetramer configurations and associated FRET efficiency values (Table S1).

ACKNOWLEDGMENTS

The optical micro-spectroscopy imaging facility used for this research was developed with support of the National Science Foundation, Major Research Instrumentation Program (Grant No. PHY-1126386 awarded to V.R.). This work was partly supported by grants from the National Science Foundation (grant number DBI-1919670) as well as the UWM Research Growth Initiative (101X396) awarded to V.R. We thank Ionel Popa for access to his protein purification facility and Claudiu Gradinaru for stimulating discussions.

REFERENCES

1. Wacker, D.; Stevens, R. C.; Roth, B. L. How Ligands Illuminate Gpcr Molecular Pharmacology. *Cell* **2017**, *170*, 414-427.
2. Latorraca, N. R.; Venkatakrishnan, A. J.; Dror, R. O. Gpcr Dynamics: Stuctures in Motion. *Chem. Rev.* **2017**, *117*, 139-155.
3. Lee, Y.; Basith, S.; Choi, S. Recent Advances in Structure-Based Drug Design Targeting Class a G Protein-Coupled Receptors Utilizing Crystal Structures and Computational Simulations. *J. Med. Chem.* **2018**, *61*, 1-46.
4. Park, P. S.; Wells, J. W. Oligomeric Potential of the M2 Muscarinic Cholinergic Receptor. *Neuropharmacology* **2004**, *90*, 537-548.

5. Maurel, D.; Comps-Agrar, L.; Brock, C.; Rives, M. L.; Bourrier, E.; Ayoub, M. A.; Bazin, H.; Tinel, N.; Durroux, T.; Prezeau, L., et al. Cell-Surface Protein-Protein Interaction Analysis with Time-Resolved Fret and Snap-Tag Technologies: Application to Gpcr Oligomerization. *Nat. Methods* **2008**, *5*, 561-567.
6. Raicu, V.; Stoneman, M. R.; Fung, R.; Melnichuk, M.; Jansma, D. B.; Pisterzi, L. F.; Rath, S.; Fox, M.; Wells, J. W.; Saldin, D. K. Determination of Supramolecular Structure and Spatial Distribution of Protein Complexes in Living Cells. *Nat. Photonics* **2009**, *3*, 107-113.
7. Patowary, S.; Alvarez-Curto, E.; Xu, T. R.; Holz, J. D.; Oliver, J. A.; Milligan, G.; Raicu, V. The Muscarinic M3 Acetylcholine Receptor Exists as Two Differently Sized Complexes at the Plasma Membrane. *Biochem. J.* **2013**, *452*, 303-312.
8. Herrick-Davis, K.; Grinde, E.; Cowan, A.; Mazurkiewicz, J. E. Fluorescence Correlation Spectroscopy Analysis of Serotonin, Adrenergic, Muscarinic, and Dopamine Receptor Dimerization: The Oligomer Number Puzzle. *Mol. Pharmacol.* **2013**, *84*, 630-642.
9. Milligan, G. The Prevelance, Maintenance, and Relevance of G Protein-Coupled Receptor Oligomerization. *Mol. Pharmacol.* **2013**, *84*, 158-169.
10. Ferre, S. The Gpcr Heterotetramer: Challenging Classical Pharmacology. *Trends Pharacol. Sci.* **2015**, *36*, 145-152.
11. Vischer, H. F.; Castro, M.; Pin, J. P. G Protein-Coupled Receptor Multimers: A Question Still Open Despite the Use of Novel Approaches. *Mol. Pharmacol.* **2015**, *88*, 561-571.
12. Levitz, J.; Habrian, C.; Bharill, S.; Fu, Z.; Vafabakhsh, R.; Isacoff, E. Y. Mechanism of Assembly and Cooperativity of Homomeric and Heteromeric Metabotropic Glutamate Receptors. *Neuron* **2016**, *92*, 143-159.
13. Whorton, M. R.; Bokoch, M. P.; Rasmussen, S. G. F.; Huang, B.; Zare, R. N.; Kobilka, B.; Sunahara, R. K. A Monomeric G Protein-Coupled Receptor Isolated in a High-Density Lipoprotein Particle Efficiently Activates Its G Protein. *Proc. Natl. Acad. Sci. U. S. A.* **2007**, *104*, 7682-7687.
14. Hern, J. A.; Baig, A. H.; Mashanov, G. I.; Birdsall, B.; Corrie, J. E. T.; Lazareno, S.; Molloy, J. E.; Birdsall, N. J. M. Formation and Dissociation of M1 Muscarinic Receptor Dimers Seen by Total Internal Reflection Fluorescence Imaging of Single Molecules. *Proc. Natl. Acad. Sci. U. S. A.* **2010**, *107*, 2693-2698.
15. Lan, T. H.; Liu, Q.; Li, C.; Wu, G.; Steyaert, J.; Lambert, N. A. Bret Evidence That Beta2 Adrenergic Receptors Do Not Oligomerize in Cells. *Sci. Rep.* **2015**, *5*, 10166.
16. Wnorowski, A.; Jozwiak, K. Homo- and Hetero-Oligomerization of B2-Adrenergic Receptor in Receptor Trafficking, Signaling Pathways and Receptor Pharmacology. *Cell. Signal.* **2014**, *26*, 2259-2265.
17. Chakraborty, H.; Chattopadhyay, A. Excitements and Challenges in Gpcr Oligomerization: Molecular Insight from Fret. *ACS Chem. Neurosci.* **2015**, *6*, 199-206.
18. Selvin, P. R. The Renaissance of Fluorescence Resonance Energy Transfer. *Nat. Struct. Mol. Biol.* **2000**, *7*, 730-734.
19. Lee, N. K.; Kapanidis, A. N.; Koh, H. R.; Korlann, Y.; Ho, S. O.; Kim, Y.; Gassman, N.; Kim, S. K.; Weiss, S. Three-Color Alternating-Laser Excitation of Single Molecules: Monitoring Multiple Interactions and Distances. *Biophys. J.* **2007**, *92*, 303-312.
20. Singh, D. R.; Cao, Q.; King, C.; Salotto, M.; Ahmed, F.; Zhou, X. Y.; Pasquale, E. B.; Hristova, K. Unliganded Epha3 Dimerization Promoted by the Sam Domain. *Biochem. J.* **2015**, *471*, 101-109.
21. Guzman, A.; Zelman-Femiak, M.; Boergermann, J. H.; Paschkowsky, S.; Kreuzaler, P. A.; Fratzl, P.; Harms, G. S.; Knaus, P. Smad Versus Non-Smad Signaling Is Determined by Lateral

Mobility of Bone Morphogenetic Protein (Bmp) Receptors. *J. Biol. Chem.* **2012**, *287*, 39492-39504.
22. Shivnaraine, R. V.; Fernandes, D. D.; Ji, H.; Li, Y.; Kelly, B.; Zhang, Z.; Han, Y. R.; Huang, F.; Sankar, K. S.; Dubins, D. N., et al. Single-Molecule Analysis of the Supramolecular Organization of the M2 Muscarinic Receptor and the Gαi1 Protein. *J. Am. Chem. Soc.* **2016**, *138*, 11583-11598.
23. Raicu, V.; Jansma, D. B.; Miller, R. J.; Friesen, J. D. Protein Interaction Quantified in Vivo by Spectrally Resolved Fluorescence Resonance Energy Transfer. *Biochem. J.* **2005**, *385*, 265-277.
24. Pisterzi, L. F.; Jansma, D. B.; Georgiou, J.; Woodside, M. J.; Tai-Chieh Chou, J.; Angers, S.; Raicu, V.; Wells, J. W. Oligomeric Size of the M2 Muscarinic Receptor in Live Cells as Determined by Quantitative Fluorescence Resonance Energy Transfer. *J. Biol. Chem.* **2010**, *285*, 16723-16738.
25. Singh, D. R.; Kanvinde, P.; King, C.; Pasquale, E. B.; Hristova, K. The Epha2 Receptor Is Activated through Induction of Distinct, Ligand-Dependent Oligomeric Structures. *Commun. Biol.* **2018**, *1*, 15.
26. Sarabipour, S.; Hristova, K. Mechanism of Fgf Receptor Dimerization and Activation. *Nat. Commun.* **2016**, *7*, 10262.
27. Stoneman, M. R.; Paprocki, J. D.; Biener, G.; Yokoi, K.; Shevade, A.; Kuchin, S.; Raicu, V. Quaternary Structure of the Yeast Pheromone Receptor Ste2 in Living Cells. *Biochim. Biophys. Acta Biomembr.* **2016**, *12*, 1456-1464.
28. Raicu, V.; Singh, D. R. Fret Spectrometry, a New Tool for the Determination of Protein Quaternary Structure in Living Cells. *Biophys. J.* **2013**, *105*, 1937-1945.
29. Mishra, A. K.; Gragg, M.; Stoneman, M. R.; Biener, G.; Oliver, J. A.; Miszta, P.; Filipek, S.; Raicu, V.; Park, P. S. Quaternary Structures of Opsin in Live Cells Revealed by Fret Spectrometry. *Biochem. J.* **2016**, *473*, 3819-3836.
30. Kobilka, B. K.; Deupi, X. Conformational Complexity of G-Protein-Coupled Receptors. *Trends Pharmacol. Sci.* **2007**, *28*, 397-406.
31. Swaminath, G.; Deupi, X.; Lee, T. W.; Zhu, W.; Thian, F. S.; Kobilka, T. S.; Kobilka, B. K. Probing the Beta-2 Adrenoceptor Binding Site with Catechol Reveals Differences in Binding and Activation by Agonists and Partial Agonists. *J. Biol. Chem.* **2005**, *280*, 22165-22171.
32. Ye, L.; Van Esp, N.; Zimmer, M.; Ernst, O. P.; Prosser, R. S. Activation of the A2a Adenosine G-Protein-Coupled Receptor by Conformational Selection. *Nature* **2016**, *533*, 265-268.
33. Miao, Y.; McCammon, J. A. Graded Activation and Free Energy Landscapes of a Muscarinic G-Protein-Coupled Receptor. *Proc. Natl. Acad. Sci. U. S. A.* **2016**, *113*, 12162-12167.
34. King, C.; Stoneman, M. R.; Raicu, V.; Hristova, K. Fully Quantified Spectral Imaging Reveals in Vivo Membrane Protein Interactions. *Integr. Biol.* **2016**, *8*, 216-229.
35. Rosenbaum, D. M.; Rasmussen, S. G.; Kobilka, B. K. The Structure and Function of G-Protein-Coupled Receptors. *Nature* **2009**, *459*, 356-363.
36. Huang, W.; Manglik, A.; Venkatakrishnan, A. J.; Laeremans, T.; Feinberg, E. N.; Sanborn, A. L.; Kato, H. E.; Livingston, K. E.; Thorsen, T. S.; Kling, R. C., et al. Structural Insights into μ-Opioid Receptor Activation. *Nature* **2015**, *524*, 315-321.
37. Kang, Y.; Zhou, X. E.; Gao, X.; He, Y.; Liu, W.; Ishchenko, A.; Barty, A.; White, T. A.; Yefanov, O.; Han, G. W., et al. Crystal Structure of Rhodopsin Bound to Arrestin by Femtosecond Xray Laser. *Nature* **2015**, *523*, 561-567.

38. Rasmussen, S. G. F.; DeVree, B. T.; Zou, Y.; Kruse, A. C.; Chung, K. Y.; Kobilka, T. S.; Thian, F. S.; Chae, P. S.; Pardon, E.; Calinski, D., et al. Crystal Structure of the B2 Adrenergic Receptor-Gs Protein Complex. *Nature* **2011**, *477*, 549-555.
39. Warne, T.; Moukhametzianov, R.; Baker, J. G.; Nehme, R.; Edwards, P. C.; Leslie, A. G. W.; Schertler, G. F. X.; Tate, C. G. The Structural Basis for Agonist and Partial Agonist Action on a Beta(1)-Adrenergic Receptor. *Nature* **2011**, *469*, 241-244.
40. Reneke, J. E.; Blumer, K. J.; Courchesne, W. E.; Thorner, J. The Carboxy-Terminal Segment of the Yeast Alpha-Factor Receptor Is a Regulatory Domain. *Cell* **1988**, *55*, 221-234.
41. Overton, M. C.; Chinault, S. L.; Blumer, K. J. Oligomerization, Biogenesis, and Signaling Is Promoted by a Glycophorin a-Like Dimerization Motif in Transmembrane Domain 1 of a Yeast G Protein-Coupled Receptor. *J. Biol. Chem.* **2003**, *278*, 49369-49377.
42. Wang, H. X.; Konopka, J. B. Identification of Amino Acids at Two Dimer Interface Regions of the Alpha-Factor Receptor (Ste2). *Biochemistry* **2009**, *48*, 7132-7139.
43. Kim, H.; Lee, B. K.; Naider, F.; J.M., B. Identification of Specific Transmembrane Residues and Ligand-Induced Interface Changes Involved in Homo-Dimer Formation of a Yeast G Protein-Coupled Receptor. *Biochemistry* **2009**, *48*, 10976-10987.
44. Umanah, G. K.; Huang, L. Y.; Maccarone, J. M.; Naider, F.; Becker, J. M. Changes in Conformation at the Cytoplasmic Ends of the Fifth and Sixth Transmembrane Helices of a Yeast G Protein-Coupled Receptor in Response to Ligand Binding. *Biochemistry* **2011**, *50*, 6841-6854.
45. Burkholder, A. C.; Hartwell, L. H. The Yeast Alpha-Factor Receptor: Structural Properties Deduced from the Sequence of the Ste2 Gene. *Nucleic Acids Res.* **1985**, *13*, 8463-8475.
46. Jenness, D. D.; Burkholder, A. C.; Hartwell, L. H. Binding of Alpha-Factor Pheromone to Saccharomyces Cerevisiae a Cells: Dissociation Constant and Number of Binding Sites. *Mol. Cell. Biol.* **1986**, *6*, 318-320.
47. Blumer, K. J.; Thorner, J. Beta and Gamma Subunits of a Yeast Guanine Nucleotide-Binding Protein Are Not Essential for Membrane Association of the Alpha Subunit but Are Required for Receptor Coupling. *Proc. Natl. Acad. Sci. U. S. A.* **1990**, *87*, 4363-4367.
48. Overton, M. C.; Blumer, K. J. G-Protein-Coupled Receptors Function as Oligomers in Vivo. *Curr. Biol.* **2000**, *10*, 341-344.
49. Overton, M. C.; Chinault, S. L.; Blumer, K. J. Oligomerization of G-Protein-Coupled Receptors: Lessons from the Yeast Saccharomyces Cerevisiae. *Eukaryot. Cell* **2005**, *4*, 1963-1970.
50. Möller, J.; Isbilir, A.; Sungkaworn, T.; Osberg, B.; Karathanasis, C.; Sunkara, V.; Grushevskyi, E. O.; Bock, A.; Annibale, P.; Heilemann, M., et al. Single-Molecule Analysis Reveals Agonist-Specific Dimer Formation of μ-Opioid Receptors *Nat. Chem. Biol.* **2020**, *16*, 946-954.
51. Kusumi, A.; Tsunoyama, T. A.; Hirosawa, K. M.; Kasai, R. S.; Fujiwara, T. K. Tracking Single Molecules at Work in Living Cells. *Nat. Chem. Biol.* **2014**, *10*, 524-532.
52. Stoneman, M. R.; Biener, G.; Ward, R. J.; Pediani, J. D.; Badu, D.; Eis, A.; Popa, I.; Milligan, G.; Raicu, V. A General Method to Quantify Ligand-Driven Oligomerization from Fluorescence-Based Images *Nat. Methods* **2019**, *16*, 493-496.
53. Stoneman, M. R.; Biener, G.; Raicu, V. Reply To: Spatial Heterogeneity in Molecular Brightness *Nat. Methods* **2020**, *17*, 276-278.
54. Park, P. S. Ensemble of G Protein-Coupled Receptor Active States. *Curr. Med. Chem.* **2012**, *19*, 1146-1154.

55. Ueda, T.; Kofuku, Y.; Okude, J.; Imai, S.; Shiraishi, Y.; Shimada, I. Function-Related Conformational Dynamics of G Protein–Coupled Receptors Revealed by Nmr. *Biophys. Rev.* **2019**, *11*, 409-418.
56. Mary, S.; Damian, M.; Louet, M.; Floquet, N.; Fehrentz, J. A.; Marie, J.; Martinez, J.; Banères, J. L. Ligands and Signaling Proteins Govern the Conformational Landscape Explored by a G Protein-Coupled Receptor. *Proc. Natl. Acad. Sci. U. S. A.* **2012**, *109*, 8304-8309.
57. Van Eps, N.; Caro, L. N.; Morizumi, T.; Kusnetzow, A. K.; Szczepek, M.; Hofmann, K. P.; Bayburt, T. H.; Sligar, S. G.; Ernst, O. P.; Hubbell, W. L. Conformational Equilibria of Light-Activated Rhodopsin in Nanodiscs *Proc. Natl. Acad. Sci. U. S. A.* [Online], 2017, p. E3268-E3275.
58. Kim, T. H.; Chung, K. Y.; Manglik, A.; Hansen, A. L.; Dror, R. O.; Mildorf, T. J.; Shaw, D. E.; Kobilka, B. K.; Prosser, R. S. The Role of Ligands on the Equilibria between Functional States of a G Protein-Coupled Receptor. *J. Am. Chem. Soc.* **2013**, *135*, 9465-9474.
59. Zimmerman, T.; Rietdorf, J.; Girod, A.; Georget, V.; Pepperkok, R. Spectral Imaging and Linear Un-Mixing Enables Improved Fret Efficiency with a Novel Gfp2-Yfp Fret Pair. *FEBS Lett.* **2002**, *531*, 245-249.
60. Tsien, R. Y. The Green Fluorescent Protein. *Annu. Rev. Biochem.* **1998**, *67*, 509-544.
61. Lippincott-Schwartz, J.; Patterson, G. H. Development and Use of Fluorescent Protein Markers in Living Cells. *Science* **2003**, *300*, 87-91.
62. Pemberton, L. F. Preparation of Yeast Cells for Live-Cell Imaging and Indirect Immunofluorescence. In *Yeast Genetics. Methods in Molecular Biology;* J. Smith, D. B., Ed. Humana Press: New York, NY, **2014**; Vol. 1205, pp 79-90.
63. Lee, B. K.; Jung, K. S.; Son, C.; Kim, H.; VerBerkmoes, N. C.; Arshava, B.; Naider, F.; Becker, J. M. Affinity Purification and Characterization of a G-Protein Coupled Receptor, Saccharomyces Cerevisiae Ste2p. *Protein Expr. Purif.* **2007**, *56*, 62-71.
64. Udden, M. M.; Finkelstein, D. B. Reaction Order of Saccharomyces Cerevisiae Alpha-Factor-Mediated Cell Cycle Arrest and Mating Inhibition. *J. Bacteriol.* **1978**, *133*, 1501-1507.
65. Biener, G.; Stoneman, M. R.; Acbas, G.; Holz, J. D.; Orlova, M.; Komarova, L.; Kuchin, S.; Raicu, V. Development and Experimental Testing of an Optical Micro-Spectroscopic Technique Incorporating True Line-Scan Excitation. *Int. J. Mol. Sci.* **2014**, *15*, 261-276.
66. Patowary, S.; Pisterzi, L. F.; Biener, G.; Holz, J. D.; Oliver, J. A.; Wells, J. W.; Raicu, V. Experimental Verification of the Kinetic Theory of Fret Using Optical Micro-Spectroscopy and Obligate Oligomers. *Biophys. J.* **2015**, *108*, 1613-1622.
67. Raicu, V. Ab Initio Derivation of the Fret Equations Resolves Old Puzzles and Suggests Measurement Strategies. *Biophys. J.* **2019**, *116*, 1313-1327.
68. Patterson, G. H.; Day, R. N.; Piston, D. W. Fluorescent Protein Spectra. *J. Cell Sci.* **2001**, *114*, 837-838.
69. Raicu, V. Extraction of Information on Macromolecular Interactions from Fluorescence Micro-Spectroscopy Measurements in the Presence and Absence of Fret. *Spectrochim. Acta A* **2018**, *199*, 340-348.
70. Raicu, V. Efficiency of Resonance Energy Transfer in Homo-Oligomeric Complexes of Proteins. *J. Biol. Phys.* **2007**, *33*, 109-127.
71. Nagy, A.; Wu, J.; Berland, K. M. Observation Volumes and Γ-Factors in Two-Photon Fluorescence Fluctuation Spectroscopy. *Biophys. J.* **2005**, *89*, 2077-2090.
72. Raicu, V.; Schmidt, W. F. Advanced Microscopy Techniques. In *G Protein-Coupled Receptor Dimers;* Herrick-Davis, K.; Milligan, G.; Di Giovanni, G., Eds.; Humana Press: Cham, 2017; pp 39-75.

73. Singh, D. R.; Raicu, V. Comparison between Whole Distribution- and Average-Based Approaches to the Determination of Fluorescence Resonance Energy Transfer Efficiency in Ensembles of Proteins in Living Cells. *Biophys. J.* **2010**, *98*, 2127-2135.
74. Mongin, O.; Porres, L.; Moreaux, L.; Mertz, J.; Blanchard-Desce, M. Synthesis and Photophysical Properties of New Conjugated Fluorophores Designed for Two Photon-Excited Fluorescence. *Org. Lett.* **2002**, *4*, 719-722.
75. Bourson, J.; Pouget, J.; Valeur, B. Ion-Responsive Fluorescent Compounds .4. Effect of Cation Binding on the Photophysical Properties of a Coumarin Linked to Monoaza-Crown and Diaza-Crown Ethers. *J. Phys. Chem.* **1993**, *97*, 4552-4557.
76. Chudakov, D. M.; Lukyanov, S.; Lukyanov, K. A. Tracking Intracellular Protein Movements Using Photoswitchable Fluorescent Proteins Ps-Cfp2 and Dendra2. *Nat. Protoc.* **2007**, *2*, 2024-2032.
77. Badali, D.; Gradinaru, C. C. The Effect of Brownian Motion of Fluorescent Probes on Measuring Nanoscale Distances by Förster Resonance Energy Transfer. *J. Chem. Phys.* **2011**, *134*, 225102.
78. Clegg, R. M. Fluorescence Resonance Energy Transfer and Nucleic Acids. *Meth. Enzymol.* **1992**, *211*, 353-388.
79. Ulbrich, M. H.; Isacoff, E. Y. Subunit Counting in Membrane-Bound Proteins. *Nat. Methods* **2007**, *4*, 319-321.
80. McAnaney, T. B.; Zeng, W.; Doe, C. F. E.; Bhanji, N.; Wakelin, S.; Pearson, D. S.; Abbyad, P.; Shi, X.; Boxer, S. G.; Bagshaw, C. R. Protonation, Photobleaching, and Photoactivation of Yellow Fluorescent Protein (Yfp 10c): A Unifying Mechanism. *Biochemistry* **2005**, *44*, 5510-5524.
81. Patterson, G. H.; Piston, D. W. Photobleaching in Two-Photon Excitation Microscopy. *Biophys. J.* **2000**, *78*, 2159-2162.
82. Stryer, L.; Haugland, R. P. Energy Transfer: A Spectroscopic Ruler. *Proc. Natl. Acad. Sci. U. S. A.* **1967**, *58*, 719-726.
83. Costa-Neto, C. M.; Parreiras-E-Silva, L. T.; Bouvier, M. A Pluridimensional View of Biased Agonism. *Mol. Pharmacol.* **2016**, *90*, 587-595.
84. Senapati, S.; Poma, A. B.; Cieplak, M.; Filipek, S.; Park, P. S. Differentiating between Inactive and Active States of Rhodopsin by Atomic Force Microscopy in Native Membranes. *Anal. Chem.* **2019**, *91*, 7226-7235.
85. Ruprecht, J. J.; Mielke, T.; Vogel, R.; Villa, C.; Schertler, G. F. Electron Crystallography Reveals the Structure of Metarhodopsin I. *EMBO J.* **2004**, *23*, 3609-3620.
86. Moukhametzianov, R.; Warne, T.; Edwards, P. C.; Serrano-Vega, M. J.; Leslie, A. G.; Tate, C. G.; Schertler, G. F. Two Distinct Conformations of Helix 6 Observed in Antagonist-Bound Structures of a Beta1-Adrenergic Receptor. *Proc. Natl. Acad. Sci. U. S. A.* **2011**, *108*, 8228-8232.
87. Singh, K. D.; Unal, H.; Desnoyer, R.; Karnik, S. S. Mechanism of Hormone Peptide Activation of a Gpcr: Angiotensin Ii Activated State of At1r Initiated by Van Der Waals Attraction. *J. Chem. Inf. Model.* **2019**, *59*, 373-385.
88. Robles, L. M.; Millán-Pacheco, C.; Pastor, N.; Del Río, G. Structure-Function Studies of the Alpha Pheromone Receptor from Yeast. *Tip Rev. Espec. En Cienc. Quim.-Biol.* **2017**, *20*, 16-26.
89. Navarro-Polanco, R. A.; Moreno Galindo, E. G.; Ferrer-Villada, T.; Arias, M.; Rigby, J. R.; Sanchez-Chapula, J. A.; Tristani-Firouzi, M. Conformational Changes in the M2 Muscarinic Receptor Induced by Membrane Voltage and Agonist Binding. *J. Physiol.* **2011**, *589*, 1741-1753.

90. Haga, K.; Kruse, A. C.; Asada, H.; Yurugi-Kobayashi, T.; Shiroishi, M.; Zhang, C.; Weis, W. I.; Okada, T.; Kobilka, B. K.; Haga, T., et al. Structure of the Human M2 Muscarinic Acetylcholine Receptor Bound to an Antagonist. *Nature* **2012**, *482*, 547-551.
91. Tateyama, M.; Kubo, Y. Binding of Gq Protein Stabilizes the Activated State of the Muscarinic Receptor Type 1. *Neuropharmacology* **2013**, *65*, 173-181.
92. Li, Y.; Shivnaraine, R. V.; Huang, F.; Wells, J. W.; Gradinaru, C. C. Ligand-Induced Coupling between Oligomers of the M2 Receptor and the Gi1 Protein in Live Cells. *Biophys. J.* **2018**, *115*, 881-895.

TOC GRAPHIC